

Article

Synthesis and Crystal and Electronic Structures of the Zintl Phase $\text{Sr}_{21}\text{Cd}_4\text{Sb}_{18}$

Kowsik Ghosh  and Svilen Bobev * 

Department of Chemistry and Biochemistry, University of Delaware, Newark, DE 19716, USA; kghosh@udel.edu
* Correspondence: bobev@udel.edu; Tel.: +1-302-831-8720

Abstract: Reported herein are the synthesis and crystal chemistry analysis of the Zintl phase $\text{Sr}_{21}\text{Cd}_4\text{Sb}_{18}$. Single crystals of this compound were grown using the Sn-flux method, and structural characterization was carried out using single-crystal X-ray diffraction. Crystal data: Monoclinic space group $C2/m$ (No. 12, $Z = 4$); $a = 18.2536(6)$ Å, $b = 17.4018(5)$ Å, and $c = 17.8979(6)$ Å, $\beta = 92.024(1)^\circ$. The structure is based on edge- and corner-shared CdSb_4 tetrahedra, which ultimately form octameric $[\text{Cd}_8\text{Sb}_{22}]$ fragments, where two symmetry-equivalent subunits are connected via a homoatomic Sb–Sb interaction. The electronic band structure calculations contained herein reveal the emergence of a direct gap between the valence and the conduction bands.

Keywords: antimonides; synthesis; crystal structure; Zintl phases

1. Introduction

Zintl phases (compounds that are formed between the alkali, alkaline-earth metals and the elements from groups 13, 14 (excluding C), and 15 (excluding N)) have drawn much research attention over the years [1–15]. While, in a classic sense, Zintl phases were only based on main-group elements, extensions of the Zintl–Klemm concept [16,17] have allowed for the inclusion of some of the rare-earth metals and some of the elements from the d-block. The chemical compositions, crystal structures, and physical properties of Zintl phases are in correlation, and this interrelationship can be easily explained by the valence rules. Succinctly—the structures of Zintl phases, binary or multinary, are rationalized in such a way that the valence electrons are transferred from less electronegative metals to the more electronegative ones. The latter use the available electrons to form covalent bonds so that a closed-shell electronic state is achieved for each constituting element. As a result, Zintl phases are typically semiconductors (or poor metals), and some phases such as BaGa_2Sb_2 [8], $\text{Yb}_{14}\text{MnSb}_{11}$ [9], and $\text{Ca}_x\text{Yb}_{1-x}\text{Zn}_2\text{Sb}_2$ [12], among others [13,14], have been recognized as promising potential thermoelectric materials.

The structures of several series of compounds in the ternary systems $AE-T-Pn$ systems ($AE = \text{Ca, Sr, Ba, Eu, and Yb}$; $T = \text{Mn, Zn, and Cd}$; $Pn = \text{As, Sb, and Bi}$) can also be understood based on the Zintl concept. As shown by our group, as well as by some other teams, ternary pnictides that are commonly referred to as “2–1–2” phases [18–21], “9–4–9” phases [22–27], “14–1–11” phases [8,9,28–34], “10–1–9” phases [35–37], and “11–1–9” phases [38–40] exhibit a very rich structural chemistry. Many of the above-mentioned compounds also have interesting magnetic and transport properties.

The subject of this paper is a compound that belongs to the series “21–4–18” [15,41–44]. This family is very diverse and encompasses three different structures. The first family member of this series, $\text{Sr}_{21}\text{Mn}_4\text{Sb}_{18}$, was reported in 2000 [15]. It remained the sole representative until 2007, when a Ca-variant was identified [44]; shortly afterwards, the discovery by our team of several other “21–4–18” compounds extended this family multifold [41–44]. Of specific note is the fact that we leveraged the similarities of the crystal chemistry of groups 7 and 12 d-block elements (half-filled and completely filled d-subshells) to obtain



Citation: Ghosh, K.; Bobev, S. Synthesis and Crystal and Electronic Structures of the Zintl Phase $\text{Sr}_{21}\text{Cd}_4\text{Sb}_{18}$. *Solids* **2023**, *4*, 344–355. <https://doi.org/10.3390/solids4040022>

Academic Editor: Sophie Guillemet-Fritsch

Received: 22 September 2023
Revised: 15 October 2023
Accepted: 6 November 2023
Published: 17 November 2023



Copyright: © 2023 by the authors. Licensee MDPI, Basel, Switzerland. This article is an open access article distributed under the terms and conditions of the Creative Commons Attribution (CC BY) license (<https://creativecommons.org/licenses/by/4.0/>).

$AE_{21}Zn_4Pn_{18}$ ($AE = Ca, Eu; Pn = As, Sb$) phases [41]; we were also the first to report on dimorphism in this family by synthesizing and characterizing β - $Ca_{21}Mn_4Sb_{18}$ [44]. Surprisingly, there is still no evidence for polymorphism in other $AE_{21}T_4Pn_{18}$ systems ($T = Mn, Zn, Cd$). The currently known “21–4–18” compounds are tabulated in Table 1.

Table 1. A list of the known (to date) “21–4–18” compounds, encompassing three different structure types.

Compound	Pearson Symbol	Space Group	Reference
$Sr_{21}Mn_4Sb_{18}$	<i>mS172</i>	$C2/m$ (No. 12)	[15]
β - $Ca_{21}Mn_4Sb_{18}$	<i>mS172</i>	$C2/m$ (No. 12)	[44]
$Ca_{21}Zn_4Sb_{18}$	<i>mS172</i>	$C2/m$ (No. 12)	[41]
$Ca_{21}Zn_4As_{18}$	<i>mS172</i>	$C2/m$ (No. 12)	[41]
$Eu_{21}Zn_4Sb_{18}$	<i>mS172</i>	$C2/m$ (No. 12)	[41]
$Eu_{21}Zn_4As_{18}$	<i>mS172</i>	$C2/m$ (No. 12)	[41]
$Eu_{21}Mn_4Sb_{18}$	<i>mS172</i>	$C2/m$ (No. 12)	[42]
$Eu_{21}Cd_4Sb_{18}$	<i>mS172</i>	$C2/m$ (No. 12)	[42]
$Eu_{21}Cd_4Bi_{18}$	<i>mS172</i>	$C2/m$ (No. 12)	[42]
$Sr_{21}Cd_4Sb_{18}$	<i>mS172</i>	$C2/m$ (No. 12)	[43]
$Sr_{21}Cd_4Bi_{18}$	<i>mS172</i>	$C2/m$ (No. 12)	This work
$Ca_{21}Mn_4Bi_{18}$	<i>mS172</i>	$C2/c$ (No. 15)	[44]
α - $Ca_{21}Mn_4Sb_{18}$	<i>mS172</i>	$C2/c$ (No. 15)	[45]
$Eu_{21}Zn_4Sb_{18}$	<i>oS344</i>	$Cmce$ (No. 64)	[41]
$Ba_{21}Cd_4Sb_{18}$	<i>oS344</i>	$Cmce$ (No. 64)	[43]

Although a great deal of knowledge on the pertinent crystal chemistry has already been gathered, it is still not clear how, for a given elemental composition, one of the three structures is always realized; i.e., the origins of the apparent structural preference for a given cation/anion combination have not been unraveled [43,44]. For example, $Sr_{21}Cd_4Bi_{18}$ crystallizes in the β - $Ca_{21}Mn_4Sb_{18}$ structure type (monoclinic space group $C2/m$ (No.12, $Z = 4$)), while $Ba_{21}Cd_4Sb_{18}$ adopts its own structure type (orthorhombic space group $Cmce$ (No. 64, $Z = 8$)) [43]. $Sr_{21}Cd_4Sb_{18}$ had been mentioned in a footnote of another paper to crystallize in the same space group as $Sr_{21}Cd_4Bi_{18}$, but the details of the structural characterization are missing [11]. This article fills this gap in our knowledge, and we report on the synthesis and crystal chemistry of $Sr_{21}Cd_4Sb_{18}$.

2. Materials and Methods

2.1. Synthesis

The elements Sr, Cd, Sb, and Sn were purchased from Sigma-Aldrich and Alfa Aesar with a purity $\geq 99.9\%$ wt. Single crystals of $Sr_{21}Cd_4Sb_{18}$ were synthesized using the Sn-flux method using techniques and procedures described in detail elsewhere [43,44]. Some of the important steps are briefly provided as follows. First, to prevent oxidation, all synthetic and post-synthetic manipulations were performed in an argon-gas-filled glove box with O_2/H_2O levels below 1 ppm or were conducted under vacuum. The elements Sr: Cd: Sb: Sn were weighed in the molar ratio of 20:4:36:70 inside an argon-filled glovebox. Although the nominal composition does not match the chemical formula, the above ratio of the elements was established on a trial-and-error basis to attain the best results. The elemental mixtures were then put into alumina crucibles, which were placed inside fused silica tubes. In each growth process, the alumina crucible was covered with quartz wool on top, and the tube was then evacuated and flame-sealed.

Heating of the sealed ampoules was carried out in programmable muffle furnaces. The best conditions, also established empirically, were as follows: (1) heating to 773 K at a rate of 100 K/h, letting the ampoules remain in these conditions for 6 h, and then heating to 1223 K at a rate of 100 K/h; (2) carrying out an equilibration step at this temperature for 32 h; and (3) cooling to 873 K at a rate of 5 K/h. The reaction products were taken out from the furnaces at this temperature, and the Sn-flux was quickly removed using a

centrifuge. Then, the tubes were brought back in the glove box and opened therein. The reaction products were irregular crystals with dark-black luster.

Note: Cadmium is a toxic metal, and experiments related to this element must be handled with extreme care! The high vapor pressure of cadmium in a high-temperature reaction may cause the sealed silica tubes to break, which could lead to potentially hazardous conditions. Therefore, all described experimental procedures have to be performed in well-ventilated environments and while taking additional precautions, such as donning personal protective equipment in case of the potential failure of the silica tubes.

2.2. Crystallographic Studies

Powder X-ray diffraction (PXRD) measurements were carried out at room temperature using a Rigaku Miniflex diffractometer (filtered Cu $K\alpha$ radiation, $\lambda = 1.5418 \text{ \AA}$) operated inside a nitrogen-filled glovebox. Small portions of the obtained single crystals were ground into powder using mortars and pestles made of agate. The data were collected between 5 and 75° in 2θ with a step size of 0.05° and a 2 s per step counting time. Analysis was carried out using the JADE 6.5 software package. It must be noted here that due to the complex structure/very large unit cell/low symmetry of the title compound, the diffraction pattern produced by the Miniflex diffractometer was not optimal; it is apparent that in order to resolve all Bragg peaks, a much-higher-resolution instrument is needed. The presence of secondary phases could not be unequivocally ruled out based on the powder diffraction patterns alone, as noted in other publications. More clear evidence for the presence of some yet unidentified phases was provided via single-crystal X-ray work.

The lack of significant differences in the PXRD measurements before and after exposure to air over a period of up to two weeks confirmed the negligible air-sensitivity of the phase over the specified period of time.

Single-crystal X-ray diffraction data for the several crystals from different batches were collected at 200 K using a Bruker APEX CCD-based diffractometer (monochromated Mo $K\alpha$ radiation with $\lambda = 0.71073 \text{ \AA}$). Suitable single crystals were selected and cut under a volume of dry Paratone-N oil to appropriate dimensions ($\leq 0.10 \text{ mm}$). After that, crystals were scooped out using MiTeGen plastic loops and transferred to a goniometer, and their quality was checked via quick scans. For the best ones, intensity data were collected under a stream of cold nitrogen at $200(2) \text{ K}$ and then processed with SAINT and SADABS software packages provided by Bruker. Crystal structures were determined via the intrinsic phasing method using SHELXT and refined using the full-matrix least-squares methods on F^2 with SHELXL [46,47], using OLEX2 as a graphical user interface [48]. Atomic coordinates were standardized using the STRUCTURE TIDY program [49]. Selected details of the data collection and other relevant crystallographic parameters for a representative crystal are given in Table 2.

Table 2. Selected crystallographic data for $\text{Sr}_{21}\text{Cd}_4\text{Sb}_{18}$ ($T = 200(2) \text{ K}$; Mo $K\alpha$, $\lambda = 0.71073 \text{ \AA}$, space group $C2/m$ (No. 12), $Z = 4$). Pearson symbol for this structure is $mS172$.

Chemical Formula	$\text{Sr}_{21}\text{Cd}_4\text{Sb}_{18}$
Formula weight	4481.12
$a/\text{\AA}$	18.2536(6)
$b/\text{\AA}$	17.4018(5)
$c/\text{\AA}$	17.8979(6)
$\beta/^\circ$	92.024(1)
$V/\text{\AA}^3$	5681.6(3)
$\rho_{\text{calc.}}/\text{g cm}^{-3}$	5.24
$\mu_{(\text{Mo-K}\alpha)}/\text{cm}^{-1}$	293.6
Collected reflections	43,869
Independent reflections	8507 [$R_{\text{int}} = 0.0579$]
Goodness-of-fit	1.11

Table 2. Cont.

Chemical Formula	Sr ₂₁ Cd ₄ Sb ₁₈
$R_1 (I > 2\sigma(I))^a$	0.0322
$wR_2 (I > 2\sigma(I))^a$	0.0499
R_1 (all data) ^a	0.0430
wR_2 (all data) ^a	0.0534
$\Delta\rho_{\max,\min}/e^- \cdot \text{\AA}^{-3}$	1.58, -2.05

^a $R_1 = \sum | |F_o| - |F_c| | / \sum |F_o|$; $wR_2 = [\sum [w(F_o^2 - F_c^2)^2] / \sum [w(F_o^2)^2]]^{1/2}$, where $w = 1 / [\sigma^2 F_o^2 + (0.0073P)^2 + (3.084P)]$ and $P = (F_o^2 + 2F_c^2) / 3$.

2.3. Electronic Band Structure Calculations

Calculations of the electronic density of states (DOS) and band structure of Sr₂₁Cd₄Sb₁₈ were carried out using the Stuttgart TB-LMTO-ASA code [50,51] with local density approximation. Experimental unit cell parameters and atomic coordinates, which are tabulated in Tables 2 and 3, respectively, were used as the input parameters in our calculations. In order to satisfy the atomic sphere approximation (ASA), the von Barth–Hedin functional was employed, and empty spheres were introduced to the calculation to satisfy the filling requirements [52]. We employed $4 \times 4 \times 4$ k -point grid for the Brillouin zone integrations to accurately calculate the Fermi surface. In the graphical representations, the Fermi level was selected as the energy reference ($E_F = 0$ eV).

Table 3. Refined atomic coordinates and equivalent isotropic displacement parameters (U_{eq} ^a) for Sr₂₁Cd₄Sb₁₈.

Sr ₂₁ Cd ₄ Sb ₁₈					
Atom	Wyckoff Site	x	y	z	$U_{eq}/\text{\AA}^2$
Sr1	8j	0.0834(1)	0.1547(1)	0.3506(1)	0.010(1)
Sr2	8j	0.0863(1)	0.1628(1)	0.1454(1)	0.009(1)
Sr3	8j	0.1119(1)	0.1205(1)	0.5767(1)	0.011(1)
Sr4	8j	0.1190(1)	0.3719(1)	0.0567(1)	0.012(1)
Sr5	8j	0.1567(1)	0.3380(1)	0.4359(1)	0.010(1)
Sr6	8j	0.2533(1)	0.3247(1)	0.2431(1)	0.010(1)
Sr7	8j	0.3660(1)	0.3694(1)	0.0601(1)	0.011(1)
Sr8	8j	0.4290(1)	0.1685(1)	0.1569(1)	0.010(1)
Sr9	8j	0.4458(1)	0.1260(1)	0.3804(1)	0.010(1)
Sr10	4i	0.2533(1)	0	0.4182(1)	0.011(1)
Sr11	4i	0.2636(1)	0	0.0925(1)	0.011(1)
Sr12	4i	0.5931(1)	0	0.2548(1)	0.012(1)
Cd1	8j	0.2656(1)	0.1201(1)	0.2480(1)	0.011(1)
Cd2	4i	0.0006(1)	0	0.7929(1)	0.012(1)
Cd3	4i	0.1572(1)	0	0.7535(1)	0.011(1)
Sb1	8j	0.0794(1)	0.3179(1)	0.2563(1)	0.009(1)
Sb2	8j	0.2571(1)	0.1980(1)	0.0971(1)	0.009(1)
Sb3	8j	0.2686(1)	0.1961(1)	0.3909(1)	0.010(1)
Sb4	8j	0.4294(1)	0.3564(1)	0.2413(1)	0.009(1)
Sb5	4i	0.0465(1)	0	0.4380(1)	0.010(1)
Sb6	4i	0.0570(1)	0	0.0565(1)	0.010(1)
Sb7	4i	0.1523(1)	0	0.2522(1)	0.009(1)
Sb8	4i	0.2499(1)	0	0.6244(1)	0.010(1)
Sb9	4i	0.3805(1)	0	0.2564(1)	0.009(1)
Sb10	4i	0.4291(1)	0	0.5334(1)	0.009(1)
Sb11	4i	0.4653(1)	0	0.0723(1)	0.010(1)
Sb12	4i	0.7400(1)	0	0.1170(1)	0.009(1)
Sb13	4h	0	0.2451(1)	1/2	0.009(1)
Sb14	4g	0	0.2444(1)	0	0.009(1)

^a U_{eq} is defined as 1/3 of the orthogonalized U_{ij} tensor.

3. Results

3.1. Synthesis

Single crystals of other “21–4–18” phases have been obtained via different solid-state synthesis methods. For instance, $\text{Ba}_{21}\text{Cd}_4\text{Sb}_{18}$ has been synthesized from stoichiometric reactions of these elements at 1273 K. The reactions have been completed in sealed Nb-containers, and the flux methods have been noted as being unsuccessful in facilitating the growth of crystals [43]. The same observations have been made with regard to $\text{Ba}_{21}\text{Cd}_4\text{Bi}_{18}$ [43]. To the contrary, the self-flux method has been successfully used to obtain crystals of $\text{Sr}_{21}\text{Cd}_4\text{Bi}_{18}$ and $\text{Eu}_{21}\text{Cd}_4\text{Bi}_{18}$. These experiments entail an excess amount of cadmium and have been conducted in open alumina crucibles [44]. Some pertinent discussion on the choice of crucibles for single-crystal growth can be followed elsewhere [53].

Molten Pb as a flux has been utilized to synthesize $\text{Eu}_{18}\text{T}_4\text{Sb}_{18}$ ($T = \text{Cd}, \text{Mn}$) [42] and $\text{A}_{21}\text{Zn}_4\text{Pn}_{18}$ ($A = \text{Ca}, \text{Eu}; \text{Pn} = \text{As}, \text{Sb}$) [41]. The first appearance of the small single crystals of $\text{Sr}_{21}\text{Cd}_4\text{Sb}_{18}$ was in a Pb-flux experiment; the identity of the phase was originally mentioned in another study, where $\text{Sr}_{21}\text{Cd}_4\text{Sb}_{18}$ crystals were a byproduct of a reaction between Sr, Cd, Sb, and Pb in a ratio of 1:1:1:2 (Pb-flux) [11]. The aforementioned reaction was repeated and carried out in a similar way, as described later on in the Synthesis section, except for the modified temperature profile. The elemental mixture was heated at 1273 K for 24 h (with a heating rate of 10 K/h), followed by cooling to 773 K with a cooling rate of 3 K/h. The molten Pb was removed via centrifugation at this temperature. We attempted to improve the crystal size by altering the reaction conditions, but the crystals remained small (sub-millimetric in size) with another phase, $\text{Sr}_{11}\text{Cd}_6\text{Sb}_{12}$ [54], as a main product. Therefore, an alternative procedure was deemed necessary, which is how we embarked on trying to use the Sn-flux method to grow crystals of $\text{Sr}_{21}\text{Cd}_4\text{Sb}_{18}$. Curiously, single crystals of the first member of the “21–4–18” family, $\text{Sr}_{21}\text{Mn}_4\text{Sb}_{18}$, were also grown by using Sn as a flux [15].

While successful for the growth of 2–3 mm crystals of $\text{Sr}_{21}\text{Cd}_4\text{Sb}_{18}$, the Sn-flux did not yield a single-phase material either. Typically, there were two major products, and crystals had to be hand-picked with tweezers under a microscope. This was possible because crystals of $\text{Sr}_{21}\text{Cd}_4\text{Sb}_{18}$ were of an irregular shape, whereas the morphology of the crystals of $\text{Sr}_{11}\text{Cd}_6\text{Sb}_{12}$ [54] corresponded to needles. This was further investigated and confirmed through single-crystal X-ray diffraction.

3.2. Structure

$\text{Sr}_{21}\text{Cd}_4\text{Sb}_{18}$ crystallizes in the monoclinic space group $C2/m$ with the same structure as $\text{Sr}_{21}\text{Mn}_4\text{Sb}_{18}$ and $\beta\text{-Ca}_{21}\text{Mn}_4\text{Sb}_{18}$ [15,44]. The structure was ascertained by single-crystal X-ray diffraction methods, and a summary of the most important crystallographic parameters can be found in Tables 2 and 3. All atoms were refined with anisotropic displacement parameters, which were rather uniform and showed no anomalies (a plot of the structure with anisotropic displacement parameters at a 95% probability level can be found in the Supporting Information). This, taken together with the low residuals and the flat difference Fourier map, is a testament to the devoid-of-disorder crystallographic arrangement. The compound $\text{Sr}_{21}\text{Cd}_4\text{Bi}_{18}$ is also known [44], and its Sb- and Bi-phases are isostructural. The contraction in the unit cell parameter of $\text{Sr}_{21}\text{Cd}_4\text{Sb}_{18}$ compared to that of the isostructural phase $\text{Sr}_{21}\text{Cd}_4\text{Bi}_{18}$ ($a = 18.510(5)$ Å, $b = 17.685(4)$ Å and $c = 18.213(4)$ Å) can be explained in terms of the difference in atomic radii between Bi and Sb.

The crystal structure is depicted in Figure 1. The details of chemical bonding in this atomic arrangement have been well described in previous publications [15,41–44]; therefore, only a brief discussion will be provided herein.

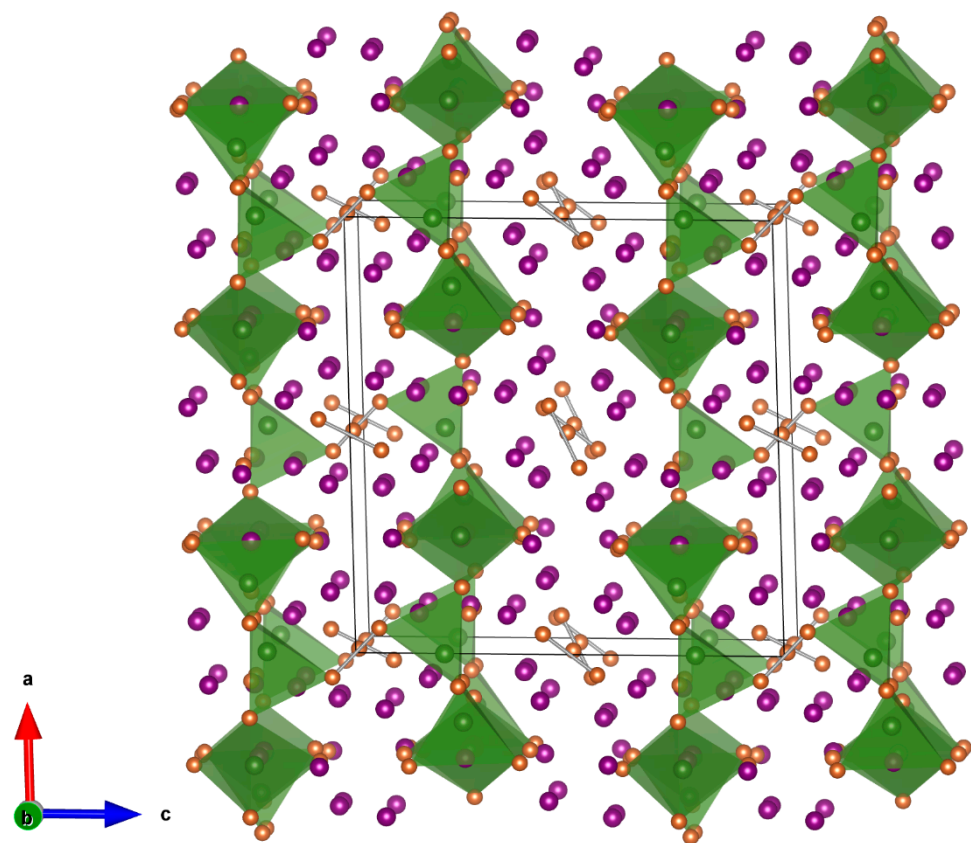


Figure 1. Schematic representation of the monoclinic crystal structure of $\text{Sr}_{21}\text{Cd}_4\text{Sb}_{18}$, viewed down the b -axis. Violet, green, and gold color atoms indicate Sr, Cd, and Sb atoms, respectively. The connectivity of the Cd-centered tetrahedra of Sb atoms is emphasized. Unit cell is outlined.

As shown in Figure 1, the structure is fairly complicated. There are a total of 29 crystallographic sites in the asymmetric unit of the structure: 12 for the Sr atoms, 3 for the Cd atoms, and 14 for the Sb atoms (Table 3). Breaking down the overall structure to molecular-like/ionic building blocks led to the following findings: in one unit cell, there are a total of 84 Sr^{2+} cations, 16 Sb^{3-} anions, six $[\text{Sb}_2]^{4-}$ dumbbells, and two $[\text{Cd}_8\text{Sb}_{22}]^{48-}$ polyanions. Since all the valence electrons are partitioned and since all the resulting ions have closed-shell electronic configurations, $\text{Sr}_{21}\text{Cd}_4\text{Sb}_{18}$ can be classified as a Zintl phase. As such, the material is expected to be a semiconductor, a notion that is also manifested in the electronic band structure, discussed in the next section. Earlier work on the electronic structures of other analogous compounds from this family also confirms this notion [43,44].

The basic Cd-Sb fragment of the structure is a $[\text{CdSb}_4]$ tetrahedron; the latter is connected via corner- and edge-sharing, forming the octameric $[\text{Cd}_8\text{Sb}_{22}]^{48-}$ cluster. Each $[\text{Cd}_8\text{Sb}_{22}]^{48-}$ is made up of two $[\text{Cd}_4\text{Sb}_{11}]^{25-}$ subunits, which are joined together by a Sb-Sb bond (Figure 2 shows a detailed view of the $[\text{Cd}_8\text{Sb}_{22}]^{48-}$ moiety). Corner-sharing tetrahedral units are connected by Sb7 atom, whereas Sb4 atoms are the connecting atoms between edge-sharing $[\text{CdSb}_4]$ tetrahedral units (Figure 2). Other “21–4–18” structures, like $\text{Ba}_{21}\text{Cd}_4\text{Bi}_{18}$ and $\alpha\text{-Ca}_{21}\text{Mn}_4\text{Sb}_{18}$, do not feature such polyanions. In the former structure (space group $Cmce$), $[\text{Cd}_4\text{Bi}_{11}]^{25-}$ akin to the $[\text{Cd}_4\text{Sb}_{11}]^{25-}$ subunits exist as standalone units and are not connected to each other. In the structure of $\alpha\text{-Ca}_{21}\text{Mn}_4\text{Sb}_{18}$ (space group $C2/c$), linear $[\text{Mn}_4\text{Sb}_{10}]^{22-}$ subunits of edge-shared $[\text{MnSb}_4]$ tetrahedra can be found.

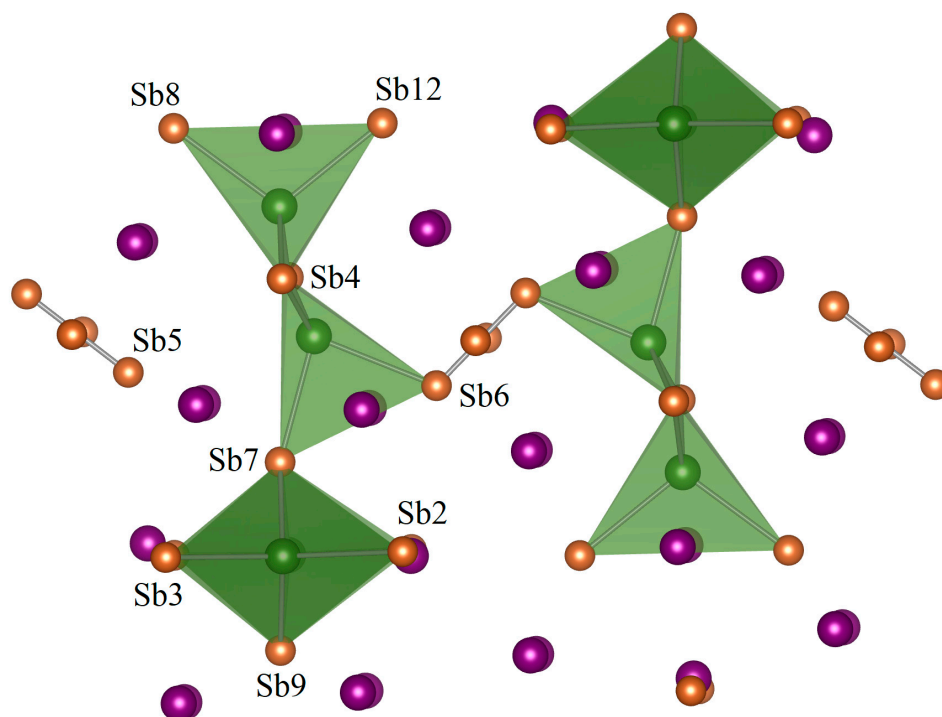


Figure 2. Close up view of $[\text{Cd}_8\text{Sb}_{22}]^{48-}$ made up of two $[\text{Cd}_4\text{Sb}_{11}]^{25-}$ subunits connected by a Sb–Sb bond. Violet, green, and gold color atoms are for Sr-, Cd-, and Sb-atoms, respectively.

4. Discussion

Within the $[\text{Sb}_2]$ dimers and $[\text{Cd}_8\text{Sb}_{22}]$ polyanions, the Sb–Sb bond lengths are within the range of 2.84–2.92 Å, while the Cd–Sb distances vary between 2.87 and 3.02 Å (Table 4). These values are close to the ones reported earlier for analogous structures [43–45] and can be compared (within less than 10%) to the sum of the Pauling covalent radii ($r_{\text{Sb}} = 1.39$ Å; $r_{\text{Cd}} = 1.38$ Å) [55]. This implies covalent bonding characteristics. The corresponding angles for the $[\text{CdSb}_4]^{10-}$ tetrahedra deviate from the ideal tetrahedral value of 109.5° , ranging from $89.71(1)^\circ$ to $125.97(2)^\circ$, matching the values in other “21–4–18” structures as well as those in ternary Sr–Cd–Sb phases such as $\text{Sr}_{11}\text{Cd}_6\text{Sb}_{12}$ [54].

Table 4. Selected interatomic distances (Å) in $\text{Sr}_{21}\text{Cd}_4\text{Sb}_{18}$.

Atom Pair	Distance/Å	Atom Pair	Distance/Å
Cd1—Sb3	2.8789(7)	Cd3—Sb8	2.9113(9)
Cd1—Sb7	2.9433(6)	Cd3—Sb12	2.9307(9)
Cd1—Sb9	2.9618(6)	Cd3—Sb4 × 2	2.9612(6)
Cd1—Sb2	3.0208(7)	Sb5—Sb5	2.841(1)
Cd2—Sb7	2.8767(9)	Sb10—Sb10	2.889(1)
Cd2—Sb4 × 2	2.8821(6)	Sb11—Sb11	2.923(1)
Cd2—Sb3	2.929(1)	Sb5—Sb5	2.841(1)

As we mentioned earlier, simple closed-shell Zintl reasoning works well for the complex structure of $\text{Sr}_{21}\text{Cd}_4\text{Sb}_{18}$. The closed-shell configurations are fully corroborated by the electronic structure calculations carried out using the TB-LMTO-ASA method [50,51]. The material’s semiconductive nature was confirmed via an inspection of the electronic band structure in momentum space, as depicted in Figure 3. In the plot, it is evident that there is a distinguishable gap between the valance and conduction bands at the Γ point. The gap between the valance (red dotted line) and conduction bands (black dotted line) is about 0.8 eV, with a direct bandgap nature. Similar semiconducting bandgaps have also been calculated for the isotypic $A_{21}\text{Cd}_4\text{Pn}_{18}$ ($A = \text{Eu}, \text{Sr}, \text{Ba}; \text{Pn} = \text{Sb}, \text{Bi}$) phases [43,44].

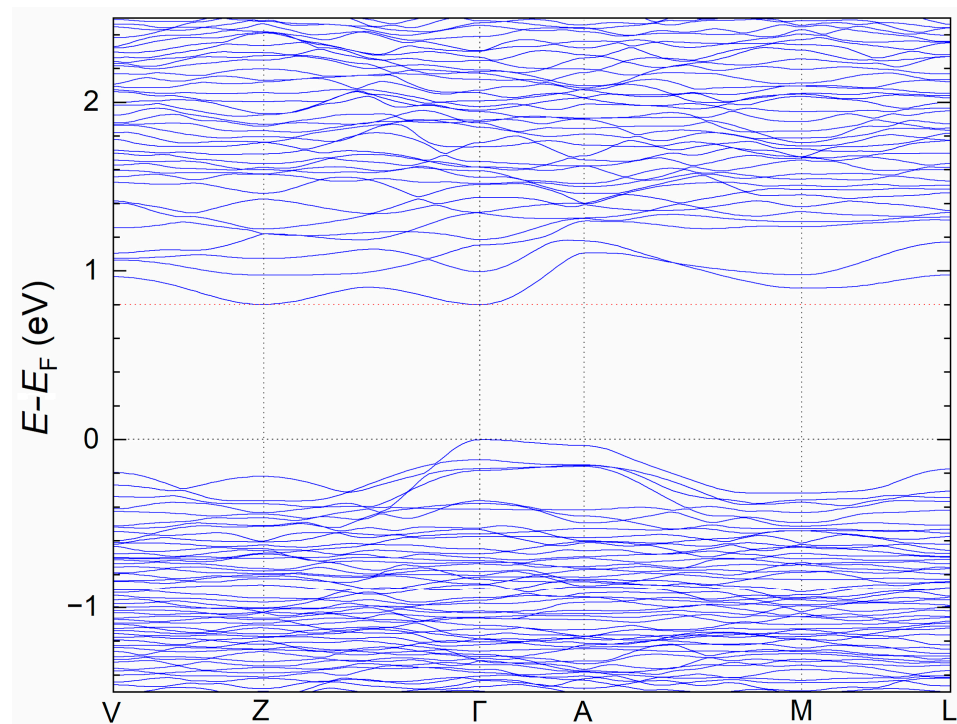


Figure 3. Electronic band structure of $\text{Sr}_{21}\text{Cd}_4\text{Sb}_{18}$ showing the energy gap between valence and conduction bands at the Γ point. Horizontal black and red dotted lines represent the top of the valence and the bottom of the conduction band, respectively.

The corresponding total and partial density of states (DOS) of $\text{Sr}_{21}\text{Cd}_4\text{Sb}_{18}$ are presented in Figure 4. The contributions from Sb are dominant in the valence band, and the contributions from Sr are dominant in the conduction band. This is indicative of a closed-shell system, as known for the typical Zintl phases [16,17]. Due to the very small number of Cd atoms, there is hardly any contribution by Cd orbitals close to the Fermi level; therefore, Cd *p*DOS is not pictured in the figure. The states below the Fermi level, while mostly contributed by Sb orbitals, still show a minor contribution from Sr orbitals. A similar phenomenon was also noticeable in the case of $\text{Sr}_{21}\text{Cd}_4\text{Bi}_{18}$ [43], where the states near the valence band maximum were dominated by Bi orbitals, with minor contributions from Sr. Such admixing of anionic and cationic orbitals indicates a small degree of covalency in the respective interactions. This means that although the fully ionic picture (84 Sr^{2+} cations, 16 Sb^{3-} anions, six $[\text{Sb}_2]^{4-}$ dumbbells, and two $[\text{Cd}_8\text{Sb}_{22}]^{48-}$ polyanions in one unit cell) allows for the easy partitioning of the valence electrons, it does not fully capture the details of chemical bonding in this complex structure.

We also considered the crystal orbital Hamilton populations (COHP) [56] and plotted them in Figure 5. In the plots, one can easily see that the atomic interactions are nearly optimized at the Fermi level, as expected for Zintl phases. No anti-bonding states for Sb–Sr interactions can be observed below the Fermi level, while some anti-bonding characteristics below the Fermi level and bonding characteristics above the Fermi level can be observed in the case of Sb–Cd interactions.

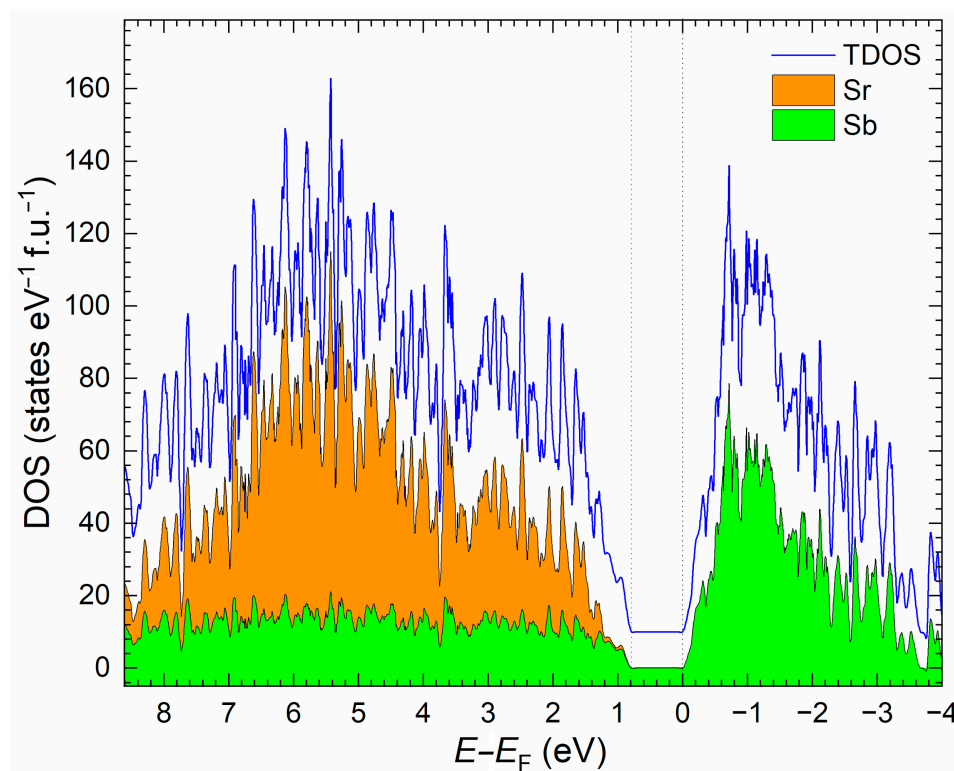


Figure 4. Atom-projected total and partial electronic density of states (DOS) of $\text{Sr}_{21}\text{Cd}_4\text{Sb}_{18}$. Black and red dotted lines represent the top of the valence and the bottom of the conduction band, respectively.

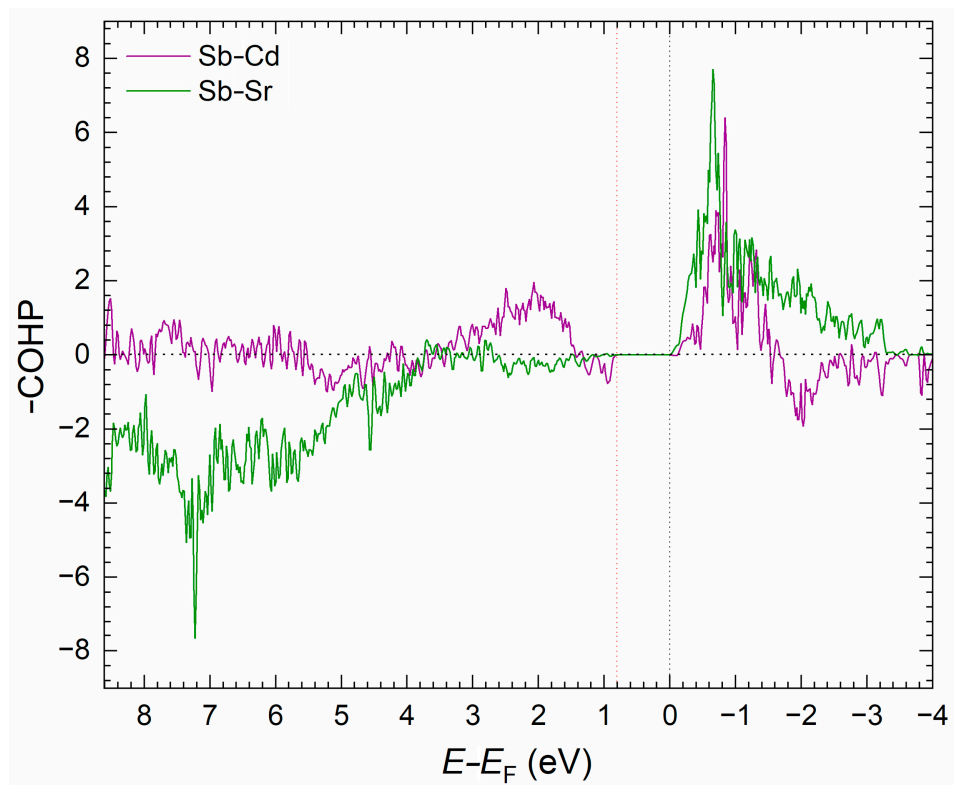


Figure 5. Crystal orbital Hamilton population (COHP) curves for Sb-Sr and Sb-Cd interactions in $\text{Sr}_{21}\text{Cd}_4\text{Sb}_{18}$. Black and red dotted lines represent the top of the valence and the bottom of the conduction band, respectively.

5. Conclusions

In this article, we have presented the crystal structure and bonding characteristics of $\text{Sr}_{21}\text{Cd}_4\text{Sb}_{18}$. Considering this compound as a Zintl phase and its semiconducting nature, it would be interesting to explore the thermoelectric properties of the bulk material in its native and doped states, as many Zintl phases have become candidate thermoelectrics in recent years. Also, since there are clear differences in the outcomes when similar synthesis procedures are used but the flux varies, it will be important to conduct a more systematic investigation of the differences between Sn-, Pb-, and Sb-fluxes in terms of their roles as plausible ways of growing crystals of “21–4–18” phases. Exploring new phases within these systems would also be desirable.

Supplementary Materials: The following supporting information can be downloaded at <https://www.mdpi.com/article/10.3390/solids4040022/s1>. Figure S1: Crystal structure of $\text{Sr}_{21}\text{Cd}_4\text{Sb}_{18}$ shown with anisotropic displacement parameters, which are shown in green, with Sb shown in red and Cd shown in blue, drawn at the 95% probability level. Sr atoms are shown in green, Sb atoms are shown in red, and Cd atoms are shown in blue.

Author Contributions: Conceptualization, S.B.; methodology, K.G.; data curation, K.G.; validation, K.G. and S.B.; formal analysis, S.B.; investigation, K.G.; resources, S.B.; writing—original draft preparation, K.G.; writing—conceptualization, K.G. and S.B.; writing—review and editing, S.B.; visualization, S.B.; supervision, S.B.; project administration, S.B.; funding acquisition, S.B. All authors have read and agreed to the published version of the manuscript.

Funding: This work was supported by the US Department of Energy (DOE) through grant DE-SC0008885.

Data Availability Statement: The corresponding crystallographic information file (CIF) has been deposited with the Cambridge Crystallographic Database Centre (CCDC) and can be obtained free of charge via <http://www.ccdc.cam.ac.uk/conts/retrieving.html> (or from the CCDC, 12 Union Road, Cambridge CB2 1EZ, UK; Fax: +44-1223-336033; E-mail: deposit@ccdc.cam.ac.uk) with the following depository number: 2296820.

Acknowledgments: The authors thank B. Saparov and J. Makongo for their earlier exploratory work on the Sr–Cd–Sb system.

Conflicts of Interest: The authors declare no conflict of interest.

References

1. Corbett, J.D. Polyanionic Clusters and Networks of the Early p-Element Metals in the Solid State: Beyond the Zintl Boundary. *Angew. Chem. Int. Ed.* **2000**, *39*, 670. [CrossRef]
2. Janka, O.; Kauzlarich, S.M. *Zintl Compounds, Encyclopedia of Inorganic and Bioinorganic Chemistry*; Wiley: Hoboken, NJ, USA, 2014; pp. 1–14.
3. Schäfer, H.; Eisenmann, B.; Müller, W. Zintl Phases: Transitions between Metallic and Ionic Bonding. *Angew. Chem. Int. Ed. Engl.* **1973**, *12*, 694–712. [CrossRef]
4. Schäfer, H. On the problem of polar intermetallic compounds: The simulation of E. Zintl’s work for the modern chemistry of intermetallics. *Ann. Rev. Mater. Sci.* **1985**, *15*, 1–41. [CrossRef]
5. Guloy, A.M. Polar Intermetallics and Zintl Phases along the Zintl Border. In *Inorganic Chemistry in Focus III*; Meyer, G., Naumann, D., Wesemann, L., Eds.; Wiley-VCH Verlag GmbH & Co: Weinheim, Germany, 2006; pp. 157–171.
6. Papoian, G.A.; Hoffmann, R. Hypervalent bonding in one, two, and three dimensions: Extending the Zintl-Klemm concept to nonclassical electron-rich networks. *Angew. Chem. Int. Ed.* **2000**, *39*, 2408–2448. [CrossRef]
7. Sevov, S.C. *Intermetallic Compounds—Principles and Practice*; Westbrook, J.H., Fleischer, R.L., Eds.; Wiley: Hoboken, NJ, USA, 2002; pp. 113–132.
8. Kim, S.-J.; Kanatzidis, M.G. A unique framework in BaGa_2Sb_2 : A new Zintl phase with large tunnels. *Inorg. Chem.* **2001**, *40*, 3781–3785. [CrossRef]
9. Brown, S.R.; Kauzlarich, S.M.; Gascoin, F.; Snyder, G.J. $\text{Yb}_{14}\text{MnSb}_{11}$: New high efficiency thermoelectric material for power generation. *Chem. Mater.* **2006**, *18*, 1873–1877. [CrossRef]
10. Ogunbunmi, M.O.; Bobev, S. Exploiting the fraternal twin nature of thermoelectrics and topological insulators in Zintl phases as a tool for engineering new efficient thermoelectric generators. *J. Mater. Chem. C.* **2023**, *11*, 8337–8357. [CrossRef]
11. Saparov, B.; Bobev, S.; Ozbay, A.; Nowak, E.R. Synthesis, structure and physical properties of the new Zintl phases $\text{Eu}_{11}\text{Zn}_6\text{Sb}_{12}$ and $\text{Eu}_{11}\text{Cd}_6\text{Sb}_{12}$. *J. Solid State Chem.* **2008**, *181*, 2690–2696. [CrossRef]

12. Gascoin, F.; Ottensmann, S.; Stark, D.; Haïle, S.M.; Snyder, G.J. Zintl phases as thermoelectric materials: Tuned transport properties of the compounds $\text{Ca}_x\text{Yb}_{1-x}\text{Zn}_2\text{Sb}_2$. *Adv. Funct. Mater.* **2005**, *15*, 1860–1864. [[CrossRef](#)]
13. Kauzlarich, S.M.; Brown, S.R.; Snyder, G.J. Zintl phases for thermoelectric devices. *Dalton Trans.* **2007**, 2099–2107. [[CrossRef](#)]
14. Snyder, G.J.; Toberer, E.S. Complex thermoelectric materials. *Nat. Mater.* **2008**, *7*, 105–114. [[CrossRef](#)] [[PubMed](#)]
15. Kim, H.; Condrón, C.L.; Holm, A.P.; Kauzlarich, S.M. Synthesis, structure, and magnetic properties of a new ternary Zintl phase: $\text{Sr}_{21}\text{Mn}_4\text{Sb}_{18}$. *J. Am. Chem. Soc.* **2000**, *122*, 10720–10721. [[CrossRef](#)]
16. Kauzlarich, S.M. *Chemistry, Structure and Bonding of Zintl Phases and Ions*; VCH: New York, NY, USA, 1998.
17. Nesper, R. The Zintl-Klemm concept—a historical survey. *Z. Anorg. Allg. Chem.* **2014**, *640*, 2639. [[CrossRef](#)]
18. Saparov, B.; Bobev, S. Isolated $[\text{ZnPn}_2]^{4-}$ chains in the Zintl phases Ba_2ZnPn_2 ($\text{Pn} = \text{As}, \text{Sb}, \text{Bi}$): Synthesis, structure, and bonding. *Inorg. Chem.* **2010**, *49*, 5173–5179. [[CrossRef](#)] [[PubMed](#)]
19. Wilson, D.; Saparov, B.; Bobev, S. Synthesis, crystal structures and properties of the Zintl phases Sr_2ZnP_2 , Sr_2ZnAs_2 , A_2ZnSb_2 and A_2ZnBi_2 ($\text{A} = \text{Sr}$ and Eu). *Z. Anorg. Allg. Chem.* **2011**, *637*, 2018. [[CrossRef](#)]
20. Chen, C.; Xue, W.; Li, S.; Zhang, Z.; Li, X.; Wang, X.; Liu, Y.; Sui, J.; Liu, X.; Cao, F.; et al. Zintl-phase Eu_2ZnSb_2 : A promising thermoelectric material with ultralow thermal conductivity. *Proc. Nat. Acad. Sci. USA* **2019**, *116*, 2831–2836. [[CrossRef](#)]
21. Ovchinnikov, A.; Bobev, S. Zintl phases with group 15 elements and the transition metals: A brief overview of pnictides with diverse and complex structures. *J. Solid State Chem.* **2019**, *270*, 346–359. [[CrossRef](#)]
22. Wu, Z.; Li, J.; Li, X.; Zhu, M.; Wu, K.; Tao, X.; Huang, B.-B.; Xia, S.-Q. Tuning the thermoelectric properties of $\text{Ca}_9\text{Zn}_{4+x}\text{Sb}_9$ by controlled doping on the interstitial structure. *Chem. Mater.* **2016**, *28*, 6917–6924. [[CrossRef](#)]
23. Liu, X.C.; Liu, K.F.; Wang, Q.Q.; Wang, M.Y.; Pan, Y.M.; Xia, S.-Q. Exploring new Zintl phases in the 9-4-9 family via Al substitution. Synthesis, structure, and physical properties of $\text{Ae}_9\text{Mn}_{4-x}\text{Al}_x\text{Sb}_9$ ($\text{Ae} = \text{Ca}, \text{Yb}, \text{Eu}$). *Inorg. Chem.* **2020**, *56*, 3709–3717. [[CrossRef](#)]
24. Bobev, S.; Thompson, J.D.; Sarrao, J.L.; Olmstead, M.M.; Hope, H.; Kauzlarich, S.M. Probing the limits of the Zintl concept: Structure and bonding in rare-earth and alkaline-earth zinc-antimonides $\text{Yb}_9\text{Zn}_{4+x}\text{Sb}_9$ and $\text{Ca}_9\text{Zn}_{4.5}\text{Sb}_9$. *Inorg. Chem.* **2004**, *43*, 5044–5052. [[CrossRef](#)]
25. Ogunbunmi, M.O.; Baranets, S.; Bobev, S. Enhanced thermoelectric performance in the Zintl antimonides $(\text{Ca}, \text{RE})_9\text{Cd}_4\text{Sb}_9$ ($\text{RE} = \text{rare-earth metal}$). Synergy between increased structural complexity and drive towards optimized chemical bonding. *Mater. Today Adv.* **2022**, *16*, 100310. [[CrossRef](#)]
26. Zhang, J.; Liu, Q.; Liu, K.-F.; Tan, W.-J.; Liu, X.-C.; Xia, S.-Q. $\text{Sr}_9\text{Mg}_{4.45(1)}\text{Bi}_9$ and $\text{Sr}_9\text{Mg}_{4.42(1)}\text{Sb}_9$: Mg-containing Zintl phases with low thermal conductivity. *Inorg. Chem.* **2021**, *60*, 4026–4033. [[CrossRef](#)]
27. Kazem, N.; Hurtado, A.; Klobes, B.; Hermann, R.P.; Kauzlarich, S.M. $\text{Eu}_9\text{Cd}_{4-x}\text{CM}_{2+x-y}\square_y\text{Sb}_9$: $\text{Ca}_9\text{Mn}_4\text{Bi}_9$ -type structure stuffed with coinage metals (Cu, Ag, and Au) and the challenges with classical valence theory in describing these possible Zintl phase. *Inorg. Chem.* **2015**, *54*, 850–859. [[CrossRef](#)] [[PubMed](#)]
28. Baranets, S.; Voss, L.; Stoyko, S.; Bobev, S. Synthesis, crystal structure and physical properties of the solid solutions $\text{Ca}_{14-x}\text{RE}_x\text{CdSb}_{11}$ ($\text{RE} = \text{La-Nd}, \text{Sm}, \text{Gd-Yb}$, $x \approx 0.85 \pm 0.15$). *J. Appl. Phys.* **2019**, *125*, 245101. [[CrossRef](#)]
29. Tan, W.-J.; Liu, Y.T.; Zhu, M.; Zhu, T.-J.; Zhao, X.-B.; Tao, X.T.; Xia, S.-Q. Structure, magnetism, and thermoelectric properties of magnesium-containing antimonide Zintl phases $\text{Sr}_{14}\text{MgSb}_{11}$ and $\text{Eu}_{14}\text{MgSb}_{11}$. *Inorg. Chem.* **2017**, *56*, 1646–1654. [[CrossRef](#)]
30. Toberer, E.S.; Cox, C.A.; Brown, S.R.; Ikeda, T.; May, A.F.; Kauzlarich, S.M.; Snyder, G.J. Traversing the metal-insulator transition in a Zintl phase: Rational enhancement of thermoelectric efficiency in $\text{Yb}_{14}\text{Mn}_{1-x}\text{Al}_x\text{Sb}_{11}$. *Adv. Funct. Mater.* **2008**, *18*, 2795–2800. [[CrossRef](#)]
31. Tan, W.; Wu, Z.; Zhu, M.; Shen, J.; Zhu, T.; Zhao, X.; Huang, B.; Tao, X.-T.; Xia, S.-Q. $\text{A}_{14}\text{MgBi}_{11}$ ($\text{A} = \text{Ca}, \text{Sr}, \text{Eu}$): Magnesium Bismuth Based Zintl Phases as Potential Thermoelectric Materials. *Inorg. Chem.* **2017**, *56*, 10576–10583. [[CrossRef](#)]
32. Vo, T.; von Allmen, P.; Cheikh, D.; Bux, S.; Fleurial, J.P. Impact of Anionic Substitution in $\text{Yb}_{14}\text{MgSb}_{11-x}\text{As}_x$ Compounds on the Electronic and Thermoelectric Properties. *J. Phys. Chem. C* **2022**, *126*, 18490–18504. [[CrossRef](#)]
33. Kastbjerg, S.; Uvarov, C.A.; Kauzlarich, S.M.; Nishibori, E.; Spackman, M.A.; Iversen, B.B. Multi-temperature Synchrotron Powder X-ray Diffraction Study and Hirshfeld Surface Analysis of Chemical Bonding in the Thermoelectric Zintl Phase $\text{Yb}_{14}\text{MnSb}_{11}$. *Chem. Mater.* **2011**, *23*, 3723–3730. [[CrossRef](#)]
34. Shang, R.; He, A.; Wille, E.L.K.; Jo, N.-H.; Fettingner, J.C.; Canfield, P.C.; Kauzlarich, S.M. Tuning the Intermediate Valence Behavior in the Zintl Compound $\text{Yb}_{14}\text{ZnSb}_{11}$ by Incorporation of $\text{RE}^{3+}[\text{Yb}_{14-x}\text{RE}_x\text{ZnSb}_{11}]$ ($0.2 \leq x \leq 0.7$), $\text{RE} = \text{Sc}, \text{Y}, \text{La}, \text{Lu}$ and Gd . *Inorg. Chem.* **2023**, *62*, 2694–2704. [[CrossRef](#)]
35. Ganguli, A.K.; Gupta, S.; Corbett, J.D. New tetragonal structure type for $\text{A}_2\text{Ca}_{10}\text{Sb}_9$ ($\text{A} = \text{Li}, \text{Mg}$). Electronic variability around a Zintl phase. *Inorg. Chem.* **2006**, *45*, 196–200. [[CrossRef](#)] [[PubMed](#)]
36. Ovchinnikov, A.; Chanakian, S.; Zevalkink, A.; Bobev, S. Ultralow Thermal Conductivity and High Thermopower in a New Family of Zintl Antimonides $\text{Ca}_{10}\text{MSb}_9$ ($\text{M} = \text{Ga}, \text{In}, \text{Mn}, \text{Zn}$) with Complex Structures and Heavy Disorder. *Chem. Mater.* **2021**, *33*, 3172–3186. [[CrossRef](#)]
37. Borgsmiller, L.; Li, Q.; Toriyama, M.Y.; Snyder, G.J. New Zintl Phase $\text{Yb}_{10}\text{MgSb}_9$ with High Thermoelectric Performance. *Adv. Energy Mater.* **2023**, *13*, 2300393. [[CrossRef](#)]
38. Bobev, S.; Fritsch, V.; Thompson, J.D.; Sarrao, J.L.; Eck, B.; Dronskowski, R.; Kauzlarich, S.M. Synthesis, structure and properties of the new rare-earth Zintl phase $\text{Yb}_{11}\text{GaSb}_9$. *J. Solid State Chem.* **2005**, *178*, 1071–1079. [[CrossRef](#)]
39. Xia, S.-Q.; Hullmann, J.; Bobev, S.; Ozbay, A.; Nowak, E.R.; Fritsch, V. Synthesis, crystal structures, magnetic and electric transport properties of $\text{Eu}_{11}\text{InSb}_9$ and $\text{Yb}_{11}\text{InSb}_9$. *J. Solid State Chem.* **2007**, *180*, 2088–2094. [[CrossRef](#)]

40. Cordier, G.; Schäfer, H.; Stelter, M. $\text{Ca}_{11}\text{InSb}_9$, eine Zintlphase mit diskreten InSb_4^{9-} Anionen. *Z. Naturforsch. B* **1985**, *40*, 868–871. [[CrossRef](#)]
41. Suen, N.-T.; Wang, Y.; Bobev, S. Synthesis, crystal structures, and physical properties of the new Zintl phases $A_{21}\text{Zn}_4\text{Pn}_{18}$ ($A = \text{Ca}, \text{Eu}; \text{Pn} = \text{As}, \text{Sb}$)—Versatile arrangements of $[\text{ZnPn}_4]$ tetrahedra. *J. Solid State Chem.* **2015**, *227*, 204–211. [[CrossRef](#)]
42. Wang, Y.; Darone, G.M.; Bobev, S. The new Zintl phases $\text{Eu}_{21}\text{Cd}_4\text{Sb}_{18}$ and $\text{Eu}_{21}\text{Mn}_4\text{Sb}_{18}$. *J. Solid State Chem.* **2016**, *238*, 303–310. [[CrossRef](#)]
43. Xia, S.-Q.; Bobev, S. Zintl phase variations through cation selection. Synthesis and structure of $A_{21}\text{Cd}_4\text{Pn}_{18}$ ($A = \text{Eu}, \text{Sr}, \text{Ba}; \text{Pn} = \text{Sb}, \text{Bi}$). *Inorg. Chem.* **2008**, *47*, 1919–1921. [[CrossRef](#)]
44. Xia, S.-Q.; Bobev, S. Diverse polyanions based on MnBi_4 and MnSb_4 tetrahedra: Polymorphism, structure, and bonding in $\text{Ca}_{21}\text{Mn}_4\text{Bi}_{18}$ and $\text{Ca}_{21}\text{Mn}_4\text{Sb}_{18}$. *Inorg. Chem.* **2007**, *46*, 874–883. [[CrossRef](#)]
45. Holm, A.P.; Olmstead, M.M.; Kauzlarich, S.M. The crystal structure and magnetic properties of a new ferrimagnetic semiconductor: $\text{Ca}_{21}\text{Mn}_4\text{Sb}_{18}$. *Inorg. Chem.* **2003**, *42*, 1973–1981. [[CrossRef](#)] [[PubMed](#)]
46. Sheldrick, G.M. SHELXT—Integrated space-group and crystal-structure determination. *Acta Cryst.* **2015**, *A71*, 3–8. [[CrossRef](#)] [[PubMed](#)]
47. Sheldrick, G.M. Crystal structure refinement with SHELXL. *Acta Cryst.* **2015**, *C71*, 3–8.
48. Dolomanov, O.V.; Bourhis, L.J.; Gildea, R.J.; Howard, J.A.K.; Puschmann, H. OLEX2: A complete structure solution, refinement and analysis program. *J. Appl. Cryst.* **2009**, *42*, 339–341. [[CrossRef](#)]
49. Gelato, L.M.; Parthé, E. STRUCTURE TIDY—a computer program to standardize crystal structure data. *J. Appl. Cryst.* **1987**, *20*, 139–143. [[CrossRef](#)]
50. Andersen, O.K. Linear methods in band theory. *Phys. Rev. B* **1975**, *12*, 3060–3083. [[CrossRef](#)]
51. Andersen, O.K.; Jepsen, O. Explicit, first-principles tight-binding theory. *Phys. Rev. Lett.* **1984**, *53*, 2571–2574. [[CrossRef](#)]
52. Von Barth, U.; Hedin, L. A local exchange-correlation potential for the spin polarized case. I. *J. Phys. C Solid State Phys.* **1972**, *5*, 1629–1642. [[CrossRef](#)]
53. Ghosh, K.; Ovchinnikov, A.; Baitinger, M.; Krnel, M.; Burkhardt, U.; Grin, Y.; Bobev, S. Lithium metal atoms fill vacancies in the germanium network of a type-I clathrate: Synthesis and structural characterization of $\text{Ba}_8\text{Li}_5\text{Ge}_{41}$. *Dalton Trans.* **2023**, *52*, 10310–10322. [[CrossRef](#)]
54. Park, S.M.; Kim, S.J. $\text{Sr}_{11}\text{Cd}_6\text{Sb}_{12}$: A new Zintl compound with infinite chains of pentagonal tubes. *J. Solid State Chem.* **2004**, *177*, 3418–3422. [[CrossRef](#)]
55. Pauling, L. *The Nature of the Chemical Bonding*, 3rd ed.; Cornell Univ. Press: Ithaca, NY, USA, 1960; p. 403.
56. Steinberg, S.; Dronskowski, R. The Crystal Orbital Hamilton Population (COHP) Method as a Tool to Visualize and Analyze Chemical Bonding in Intermetallic Compounds. *Crystals* **2018**, *8*, 225. [[CrossRef](#)]

Disclaimer/Publisher’s Note: The statements, opinions and data contained in all publications are solely those of the individual author(s) and contributor(s) and not of MDPI and/or the editor(s). MDPI and/or the editor(s) disclaim responsibility for any injury to people or property resulting from any ideas, methods, instructions or products referred to in the content.